Chapter 9

CREEP

The creep behavior of MMCs is of great significance, since in many structural and non-structural applications, these materials will be subjected to constant stress (or strain) for long periods of time, at temperature above half of the homologous temperature (homologous temperature is the temperature of interest divided by melting point, both in K; i.e., T/T_m). Most materials exhibit three distinct stages of creep: (i) primary creep, (ii) secondary or steady-state creep, and (iii) tertiary creep. In primary creep, the strains are relatively small. In the secondary or steady-state regime, a linear relationship exists between the strain and time (constant strain rate). This is believed to be a result of the combination of hardening and recovery mechanisms during creep. Finally, in the tertiary regime, the material undergoes cavitation and void growth, which is manifested in terms of a very rapid increase in strain with time.

In general, the steady creep rate, $\dot{\varepsilon}_s$, is described by a general expression called the Mukherjee-Bird-Dorn relation (Mukherjee et al., 1964):

$$\dot{\varepsilon}_s = \frac{AGbD}{kT}\left(\frac{b}{d}\right)^p\left(\frac{\sigma}{G}\right)^n$$

where σ is the applied stress, T is the temperature in kelvin, G is the shear modulus, b is the Burgers vector, d is the average grain size, p is the inverse grain size exponent, n is the stress exponent, D is the diffusion coefficient of the material, k is the Boltzmann's constant, and A is a dimensionless constant. The value of the stress exponent can usually be correlated with a particular creep mechanism (e.g., n ~ 4-5 for dislocation climb). The diffusion coefficient, D, is given by:

$$D = D_0 \exp\left(\frac{-Q_D}{RT}\right)$$

where D_0 is the pre-exponential constant, R is the universal gas constant, and Q_D is the activation energy for creep, which is often equal to the activation energy for diffusion. For a detailed discussion on the fundamentals of creep, the reader is referred to texts such as Evans and Wilshire (1993) and Meyers and Chawla (1999).

In general, the addition of high stiffness reinforcement greatly increases the creep resistance over that of unreinforced alloys. The addition of the reinforcement also changes the creep deformation mechanisms, relative to the pure matrix. A schematic of typical creep curves (strain versus time) for MMCs with continuous and discontinuous reinforcement, is shown in Fig. 9.1 (Lilholt, 1991). Composites with continuous fibers exhibit a short primary creep regime, followed by a long steady-state regime, Fig. 9.1. This behavior can be predicted by simple viscoelastic models, such as an isostrain model, where the matrix is modeled as the viscous component and the fiber is elastic. In the case of discontinuous reinforcement (short fibers or particles), a more typical creep curve is observed, with three distinct creep regimes, Fig. 9.1, since the degree of load transfer is not as high as that for continuous fibers.

9.1 CONTINUOUS FIBER REINFORCED MMCs

The creep strength of continuous fiber MMCs is usually significantly higher than that of the unreinforced alloy. Figure 9.2(a) shows creep strain versus time for Ti-6Al-4V/SiC_f composite at temperatures ranging between 430 and 650°C (Leyens et al., 2003). As mentioned above, the creep curves exhibit

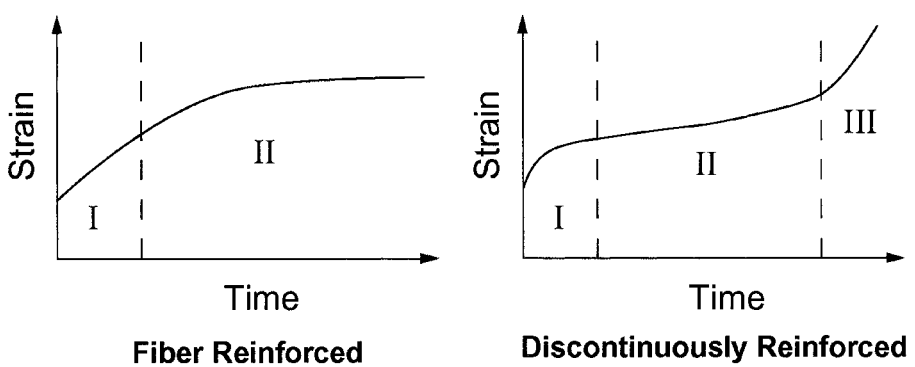

Fig. 9.1 Schematic of creep strain versus time for fiber reinforced and discontinuously reinforced MMCs (after Lilholt, 1991). The three stages of creep are (I) primary creep, (II) steady-state creep, and (III) fast fracture.

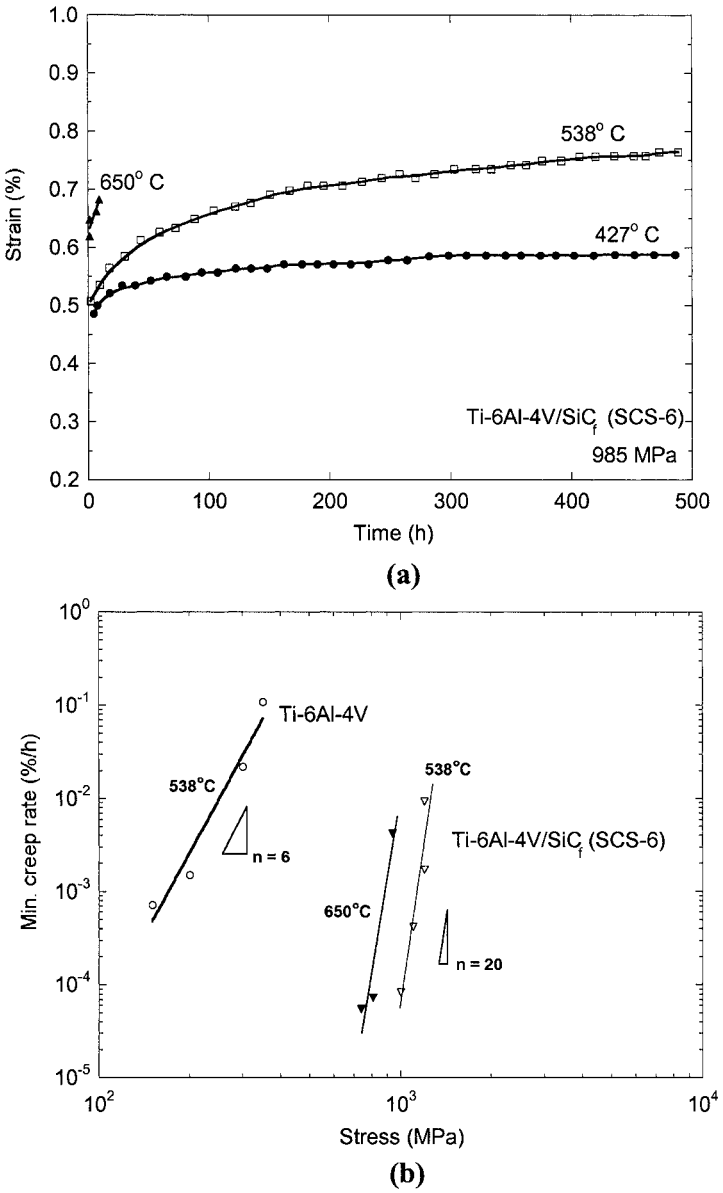

Fig. 9.2 Creep behavior of Ti-6Al-4V/SiC_f composite versus the unreinforced alloy: (a) creep strain versus time plots for temperatures ranging between 430 and 650°C and (b) steady-state creep rate versus stress. The MMC exhibits significantly higher creep resistance, but much higher creep stress exponent, n, (after Leyens et al., 2003).

two stages during creep. At the highest temperature, 650°C, the creep strain increases exponentially with time. A plot of creep strain rate, $\dot{\varepsilon}$, versus stress, σ, Fig. 9.2(b), shows that a much higher stress is required to induce a given creep strain in the composite, relative to the unreinforced alloy. The stress exponent, for the composite, however, is much larger (n ~ 20 for the composite, vis-à-vis n ~ 6 for the unreinforced alloy). The reasons for the anomalously high values of the stress exponent in the composite are explained later in this chapter. In general, off-axis creep results in poorer creep resistance (Ohno et al., 1994). At 45° large-scale shear deformation takes place in the matrix, while at 90° (transverse loading) interfacial debonding results in creep fracture.

Bullock et al. (1977) studied the behavior of directionally solidified *in situ* composites of Ni-Ni_3Al-Cr_3C_2. The creep rate was found to be inversely proportional to the scale of the eutectic microstructure, i.e., the mean fiber radius, λ. The Hall-Petch relation was modified for creep rate and written as:

$$\log\dot{\varepsilon} = \log\dot{\varepsilon}_{\infty} + K\lambda^{-\frac{1}{2}}$$

where $\dot{\varepsilon}$ is the creep rate, $\dot{\varepsilon}_{\infty}$ is the creep rate for $\lambda = \infty$, and K is a constant. A comparison of the experimentally-determined creep rates and the model prediction is presented in Fig. 9.3, showing reasonable agreement.

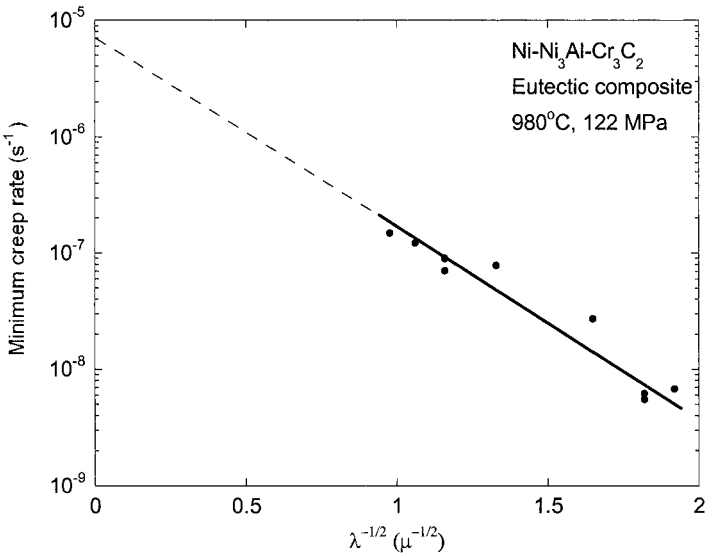

Fig. 9.3 Minimum creep rate versus inverse square root of fiber radius of directionally solidified *in situ* composites of Ni-Ni_3Al-Cr_3C_2 (after Bullock et al., 1977). The creep rate follows a modified Hall-Petch relationship.

The evolution of load transfer during creep, from the creeping matrix to the rigid reinforcement (most fibers do not creep at temperatures at which the metal matrix creeps), has an important influence on the creep of the composite. As the matrix creeps, an increasing fraction of the load is transferred to the fibers, Fig. 9.4(a). Upon unloading, the load in the fiber and matrix decrease. The stress in the matrix, however, dips below zero and then increases slightly. This phenomenon is termed creep recovery. A three dimensional finite element model of a fiber reinforced MMC (E_m = 60 GPa, E_f = 470 GPa, 15 vol.% of fibers, with a matrix deforming by power-law creep) illustrates this behavior very nicely, Fig. 9.4(b) (Sørensen et al., 1992).

The gradual transfer of load from the matrix to the fibers can be modeled by assuming that the fiber behaves elastically and that the matrix follows power law creep ($\dot{\varepsilon} = A\sigma^n$). Then the creep rate of the composite is given by:

$$\dot{\varepsilon}_c = \frac{A\sigma^n \left[1 - \frac{\dot{\varepsilon}}{\dot{\varepsilon}_\infty}\right]^n}{\left[1 + \frac{V_f E_f}{V_m E_m}\right] V_m^n}$$

where $\dot{\varepsilon}_\infty$ is the asymptotic creep strain, which is achieved when all of the load has been transferred to the fibers. It is given by:

$$\dot{\varepsilon}_\infty = \frac{\sigma_c}{V_f E_f}$$

The creep behavior of the composite is also dependent on whether the matrix creeps faster than the matrix, $\dot{\varepsilon}_m > \dot{\varepsilon}_f$, or vice versa, Fig. 9.5. In the case of matrix creeping faster, one may expect the fibers to fracture first. In the reverse scenario, $\dot{\varepsilon}_f > \dot{\varepsilon}_m$, the matrix should crack first, allowing the fibers to bridge the crack.

Lilholt (1985) proposed analytical models for predicting the creep behavior of fiber reinforced MMCs. He considered two cases: (a) fiber elastic and matrix creeping, and (b) both and fiber and matrix creeping. Load transfer to the fibers was modeled using a modified shear-lag theory, with the matrix between the fibers deforming by shear, and matrix at the fiber ends deforming in tension. While pure metals undergo power-law creep, the local stress in the matrix of the composite is significantly higher, so an

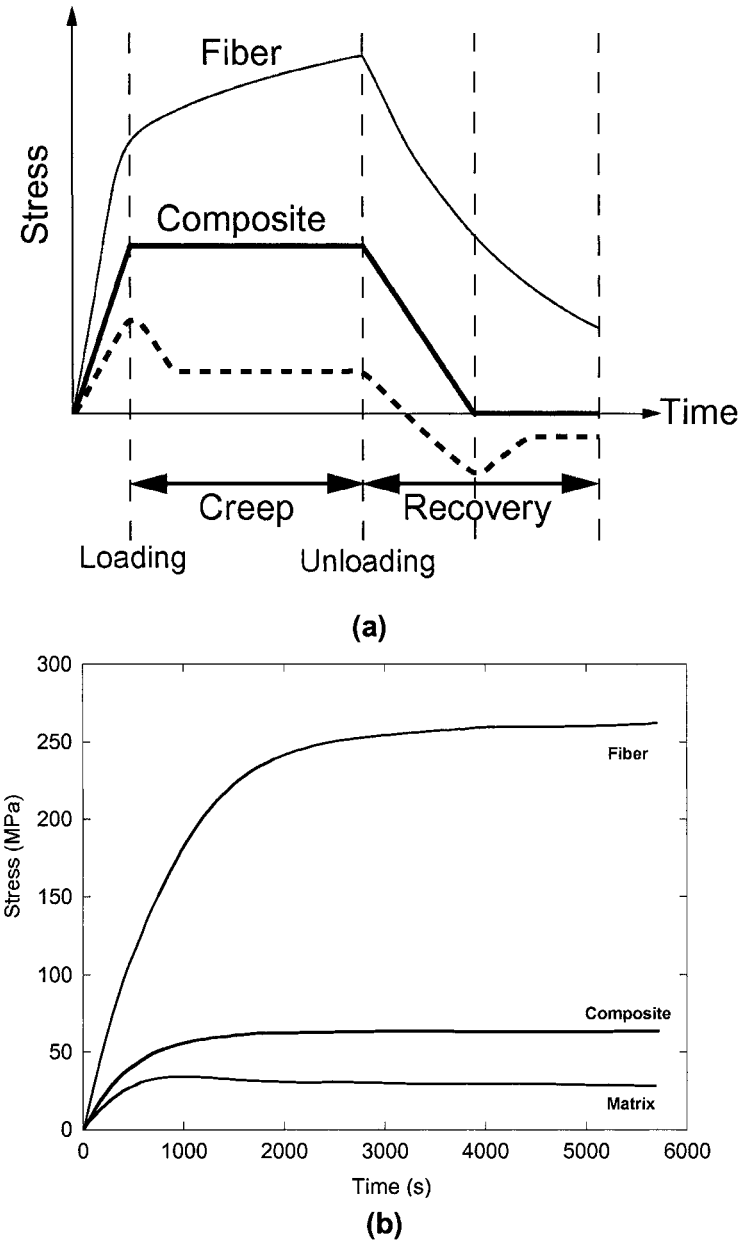

Fig. 9.4 Evolution of load transfer during creep, from the creeping matrix to the rigid reinforcement: (a) schematic of experimental behavior and (b) three-dimensional finite element model (after Sørensen et al., 1992). As the matrix creeps, an increased fraction of the load is transferred to the fibers. Upon unloading, slight creep recovery in the matrix takes place.

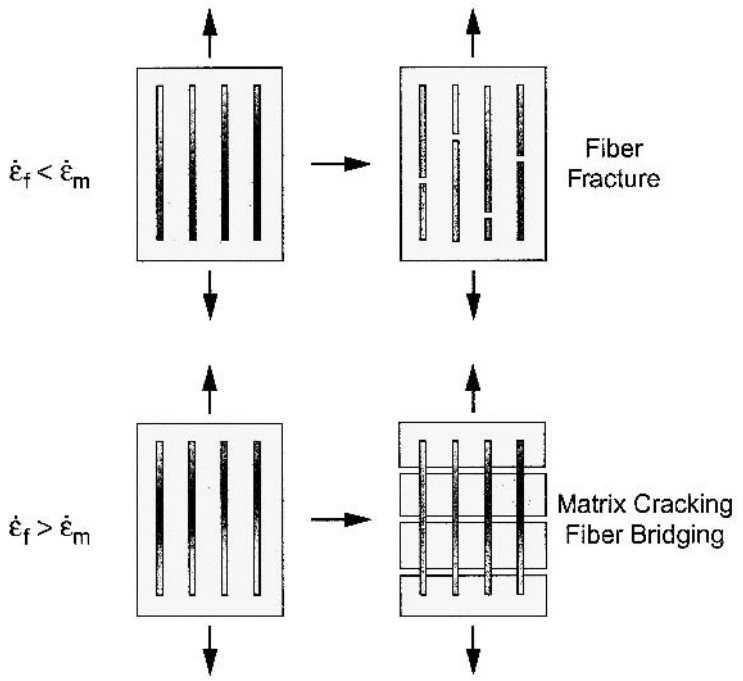

Fig. 9.5 Creep behavior of fiber reinforced MMC. When the matrix creeps faster than the matrix, $\dot{\varepsilon}_m > \dot{\varepsilon}_f$, the fibers fracture first. For $\dot{\varepsilon}_f > \dot{\varepsilon}_m$, the matrix cracks first, allowing the fibers to bridge the crack.

exponential law describing matrix creep was deemed to be more appropriate (at these stresses the power law breaks down). The exponential law was given by:

$$\dot{\varepsilon} = \dot{\varepsilon}_o \exp\left[-\frac{Q}{RT}\left(1-\frac{\sigma}{\sigma_o}\right)\right]$$

where σ is the applied stress, $\dot{\varepsilon}$ is the creep rate, $\dot{\varepsilon}_o$ is a constant, Q is the activation energy for creep (taken here as the activation energy for dislocation glide), and σ_o is the strength of the glide obstacles at 0 K. The total composite strength was modeled as a sum of the following components:

$$\sigma_c = \sigma_m + \sigma_{th} + <\sigma>$$

where σ_m is the creep strength of the matrix, σ_{th} is a threshold stress for Orowan bowing of dislocations, and $<\sigma>$ is a mean stress that is directly proportional to the applied strain. Good agreement was obtained with

experimental results on model composites, such as Ni/W_f and $Ni/NiAl_f,Cr_3C_{2f}$.

Goto and McLean (1989, 1991) modeled the creep behavior of continuous and short fiber reinforced MMCs, based on the nature of the fiber/matrix interface, Fig. 9.6. If the fiber/matrix interface is completely incoherent, Orowan loops will stop at the interface and climb parallel to the fiber length. This results in extensive recovery and very little hardening at the interface. It also results in extensive strain relaxation at the interface and contributes to slipping of the boundary. For the case of the completely coherent boundary, two cases exist. If the modulus of the matrix is greater than that of the fiber,

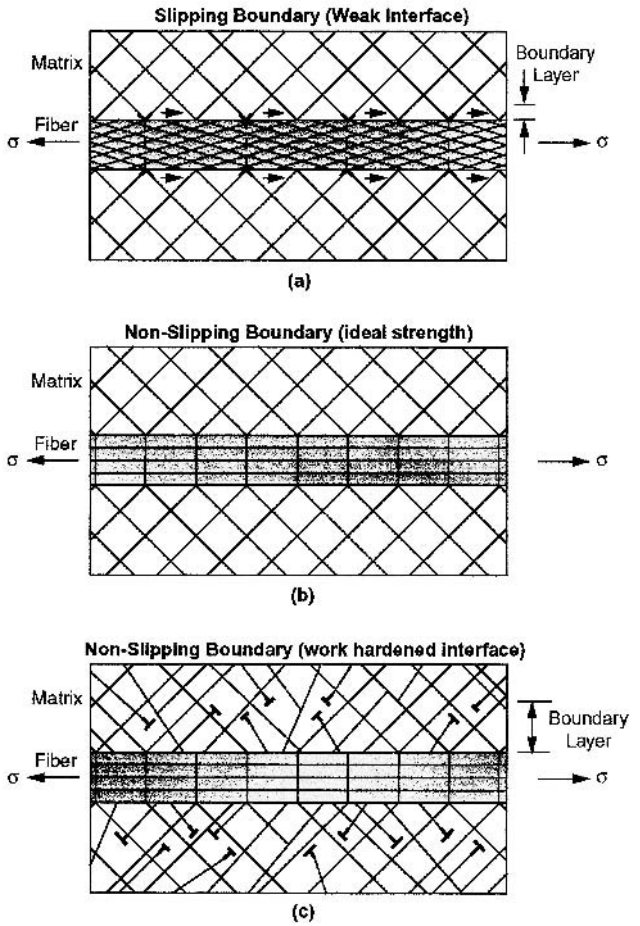

Fig. 9.6 Types of fiber/matrix interface used in modeling creep behavior (after Goto and McLean, 1989, 1991): (a) weak interface, (b) ideal strength interface, and (c) work hardened interface.

i.e., $E_m > E_f$, the dislocations are attracted to the boundary, the coherency is retained, although some slippage may take place. For the case of $E_m < E_f$, the dislocation loops are repelled from the fiber and a work hardened zone is created that is not conducive to interface slipping. The results of their model showed that the work hardened boundary temporarily carries a large fraction of the load, prior to transferring it to the fibers. This results in an enhancement in creep life. The case for a weak interface did not appear to have a significant effect on creep behavior in continuous fibers, although it did affect the short fiber behavior.

Aspects of fiber fracture and interfacial debonding were also analyzed by Lee et al. (1995). These authors conducted a parametric analysis of the creep behavior of SCS-6 fiber reinforced Ti matrix composites. They used an iterative computer simulation to determine the stress in the fiber and matrix at a given time. Models with single and multiple fibers were considered. Figure 9.7 shows two examples of numerical model predictions. Figure 9.7(a) shows the case of composites with (i) no fiber fracture, (ii) fiber fracture but no interfacial debonding, and (iii) fiber fracture with interfacial debonding. As expected, the material with fiber fracture and interfacial debonding exhibits the highest creep strain, for a given time, while the composite with no fiber fracture is the most creep resistant. The effect of interfacial strength is illustrated in Fig. 9.7(b). Note that with increasing interfacial strength, creep of the matrix is more constrained, so the overall composite creep rate is lower.

9.2 DISCONTINUOUSLY REINFORCED MMCs

Dlouhy et al. (1993, 1995) examined the creep behavior of Al_2O_3 short fiber reinforced Al7Si3Cu alloy matrix composites, processed by squeeze casting. Three major mechanisms for creep damage were proposed: (i) load transfer to the fibers through a work hardened zone (WHZ) some distance from the fiber/matrix interface; (ii) diffusional/recovery mechanisms that result in a decrease in dislocation density in the WHZ; and (iii) multiple fiber fracture. The WHZ develops in the primary creep regime, which contributes to significant load transfer to the fibers. The recovery process results from dislocations moving to the fiber ends by combined climb and glide processes, Fig. 9.8. Figure 9.9 shows a comparison of the dislocation structure, in the matrix of the composite, in the as-processed condition and after creep deformation at 623 K, stress of 40 MPa, and rupture at 1.7% total strain. Note the much higher dislocation density at the fiber/matrix interface after creep. The addition of Mg to the alloy resulted in the formation of

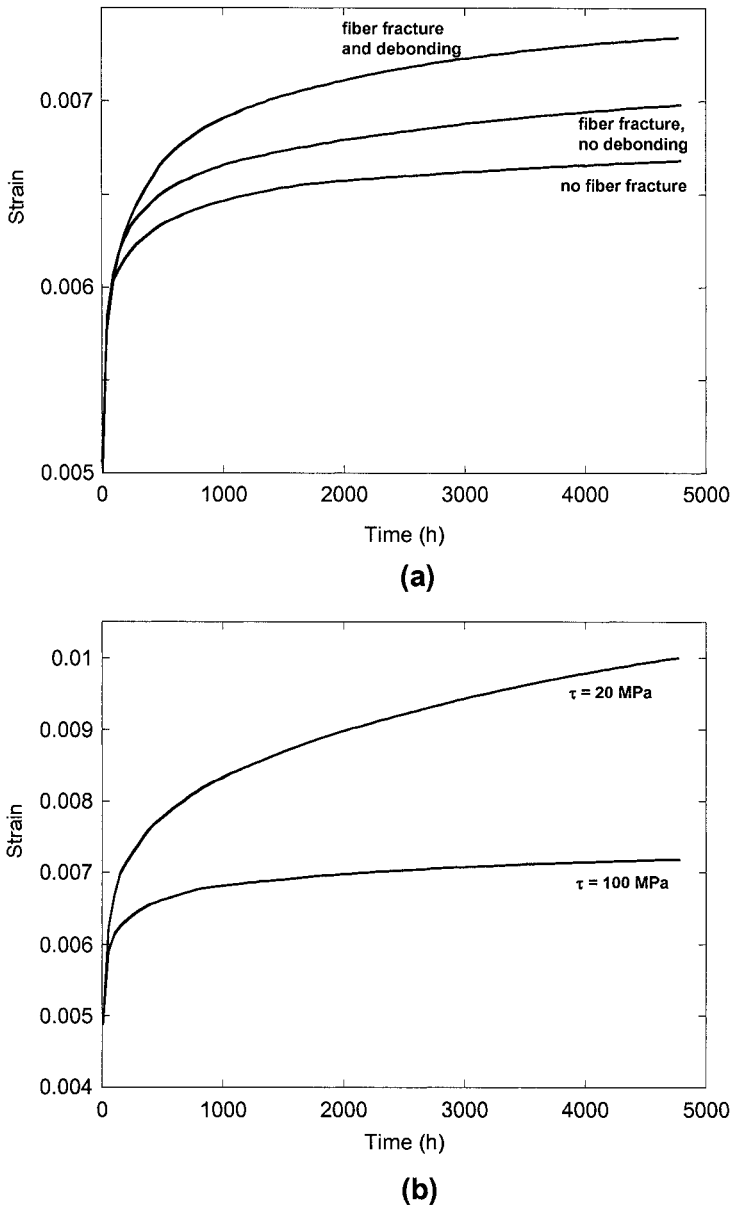

Fig. 9.7 Numerical analysis of creep behavior of SCS-6 fiber reinforced Ti matrix composite (after Lee et al., 1995): (a) effect of fiber fracture and debonding – fracture and debonding increase the creep rate of the composite; and (b) effect of interfacial shear strength, τ – increasing interface strength increases the constraint on the matrix, which lowers the creep rate of the composite.

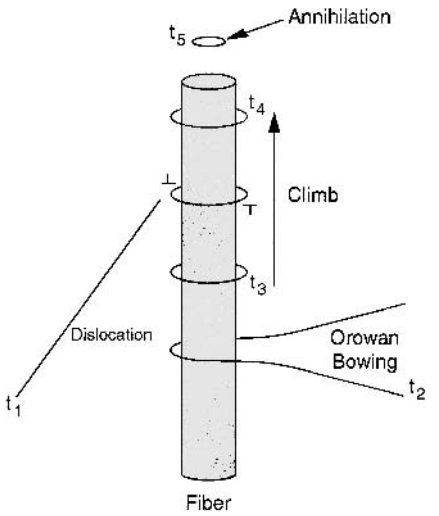

Fig. 9.8 Proposed mechanism for creep deformation in a fiber reinforced MMC (after Dlouhy et al., 1993, 1995). A dislocation bows around the fiber. The dislocation segment at the interface climbs parallel to the fiber axis and is annihilated at the fiber ends.

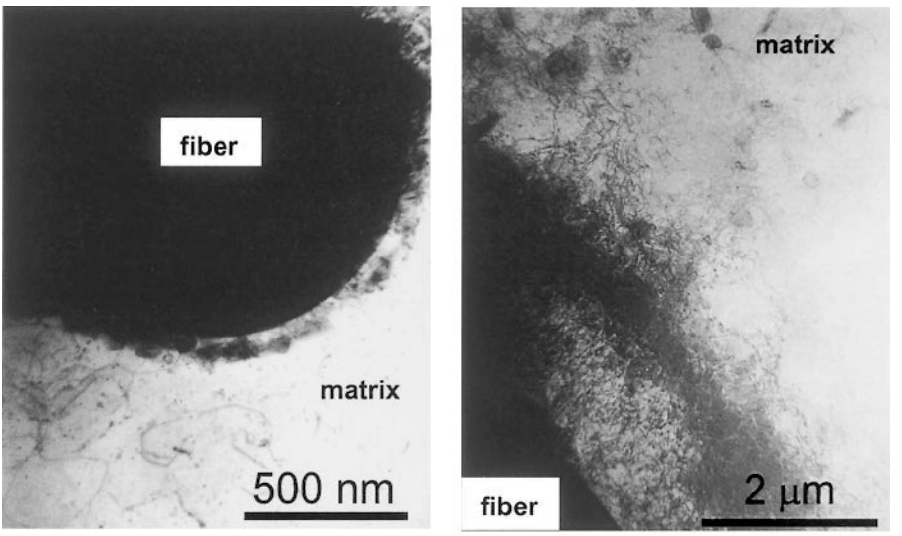

(a) **(b)**

Fig. 9.9 Comparison of dislocation in the matrix of the composite in (a) the as-processed condition and (b) after creep deformation at 623 K, 40 MPa, and rupture at 1.7% total strain (courtesy of A. Dlouhy and G. Eggeler). Note the enhanced dislocation density at the fiber/matrix interface after creep.

intermetallic particles at the fiber/matrix interface (Dlouhy et al., 1993). The proposed effect of the particles at the interface was a longer effective path for recovery, and thus, an increase in creep strength. Eventually, the stress concentration caused by dislocation pile-up at the fiber/matrix interface results in fiber fracture, see Figs. 9.10 and 9.11. This also aids in recovery because of matrix diffusion at the fiber cracks. Fiber fracture and the increase in recovery contribute to the onset of tertiary creep. By using springs (elastic behavior) and dashpots (viscoelastic behavior) to represent individual components of the material behavior, excellent correlation with the experiment was obtained.

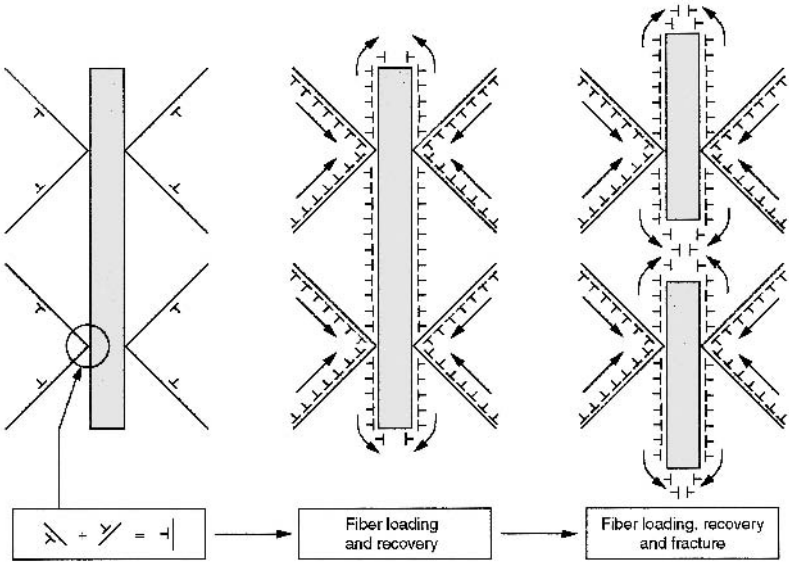

Fig. 9.10 Effect of dislocation pile-up at the fiber/matrix interface during creep (after Dlouhy et al., 1993). The stress concentration caused by dislocation pile-up results in fiber fracture, aiding in recovery because of diffusion at the fiber cracks.

Fig. 9.11 Fiber fracture (indicated by arrows) in Al_2O_3 short fiber reinforced Al7Si3Cu alloy matrix composite during creep (courtesy of A. Dlouhy and G. Eggeler). The loading axis is horizontal.

While short fibers or whiskers provide significant creep strengthening, particulate reinforcement has also been used to enhance creep resistance. Nieh (1984) studied the creep behavior of 6061/SiC/20_p and 6061/SiC/20_w, and compared it to that of the unreinforced 6061 alloy, Fig. 9.12. He noted a much higher creep resistance in the composite with an accompanying higher sensitivity to applied stress (much higher stress exponent n). Enhanced creep resistance was also obtained with the higher aspect ratio whiskers than with particles, presumably due to more effective load transfer from the matrix to the whisker of high stiffness and large aspect ratio. Webster (1982) also characterized the creep behavior of the matrix alloy and its whisker reinforced composite with increasing temperature. At intermediate temperatures (500-720K) the strength was controlled by the whiskers, as the load was transferred to the high modulus and high aspect ratio reinforcement. The strength becomes matrix-controlled at very high temperatures (720-900 K), perhaps due to increasingly lower interfacial shear strength and lower efficiency in load transfer to the whisker reinforcement. Evidence of creep cavitation, predominantly at reinforcement particle clusters, has also been observed (Whitehouse et al., 1998).

Krajewski et al. (1993, 1995) studied the creep behavior of 2219/TiC/15_p-T6 composites, and compared it to that of the unreinforced alloy. They found that the precipitate structure in the matrix of the composite had a dominant effect on controlling creep rate. The composite had a finer interprecipitate

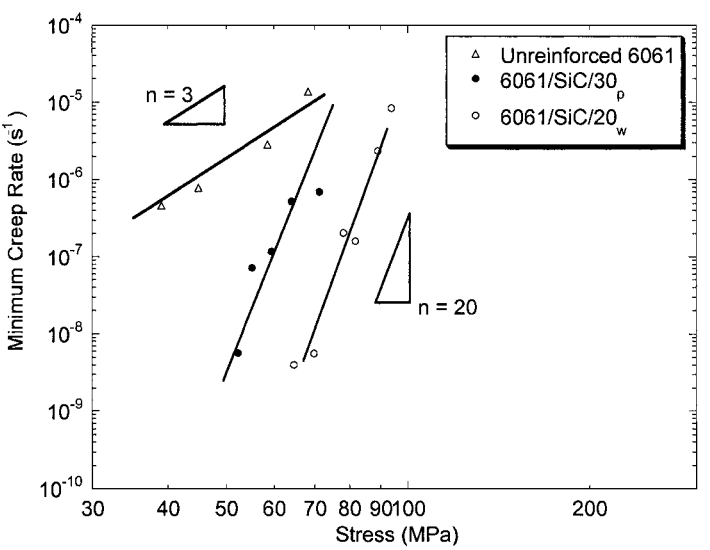

Fig. 9.12 Creep behavior of 6061/SiC particle and whisker reinforced composites (after Webster, 1982). Notice the higher creep resistance of the whisker reinforced material, due to more effective load transfer to the reinforcement.

spacing than that of the unreinforced alloy, due to indirect strengthening (see Chapter 7). Figure 9.13(a) shows the unreinforced precipitate structure in the matrix of the composite. The precipitates exhibit characteristic needle-like morphology observed in Al-Cu and Al-Cu-Mg alloys. After creep deformation at 250°C and 75 MPa, the precipitates serve as barriers for dislocation motion, Fig. 9.13(b).

In unreinforced aluminum alloys, Sherby et al. (1977) showed that the creep behavior was proportional to the substructure grain size, λ, to the third power, i.e., λ^3. They also concluded that in materials where a subgrain size during creep was relatively constant, the steady-state creep rate was better described by a stress exponent of 8, rather than the conventional value of 5 for dislocation creep. Thus, the following equation was used to describe the steady state creep rate in pure aluminum:

$$\dot{\varepsilon} = S\left(\frac{D_{eff}}{b^2}\right)\left(\frac{\lambda}{b}\right)^3\left(\frac{\sigma}{E}\right)^8$$

where S is a constant, E is the Young's modulus of the materials, and D_{eff} is the effective diffusivity for creep. Krajewski et al. (1993, 1995) also found that the creep rate in 2219/TiC/15_p composites was proportional to the interprecipitate spacing, in the matrix, to the third power. They rationalized this behavior by postulating that a substructure is formed due to the presence of the reinforcement, and the size of the substructure may be controlled by the interprecipitate spacing.

The anomalously high values of the stress exponent, n, and activation energy, Q, can be rationalized by using the concept of a threshold stress (Webster, 1982; Nieh, 1984, Nardone and Strife, 1987). Nardone and Strife (1987) used the concept of a threshold stress, σ_R, for creep deformation in composites. This theory was originally used to explain the high values for Q and n in dispersion-strengthened alloys (Davies et al., 1973; Parker and Wilshire, 1975; Nardone and Tien, 1986, Kerr and Chawla, 2004). By introducing the threshold stress, the general steady-state creep rate is modified to:

$$\dot{\varepsilon}_{ss} = A\left(\frac{\sigma - \sigma_R}{E}\right)^n \exp\left(\frac{-Q}{RT}\right)$$

where A is a constant, E is the elastic modulus of the composite, and Q is the activation energy. A methodology for determining the threshold stress from

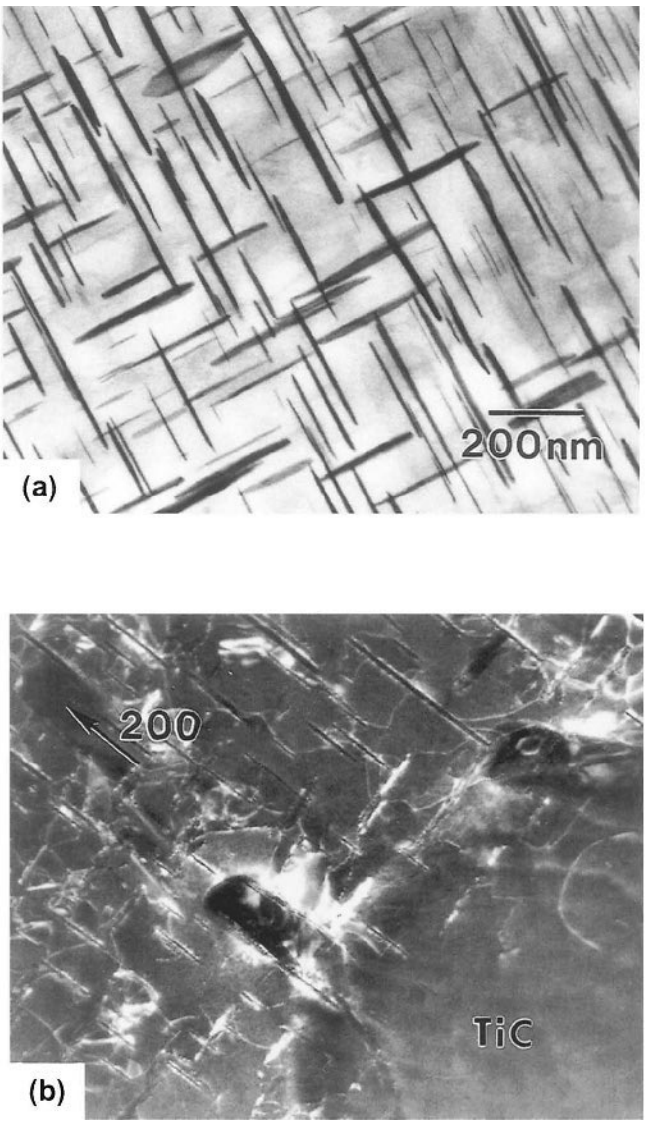

Fig. 9.13 Precipitate structure in the matrix of a 2219/TiC/15_p-T6 composite (after Krajewski et al., 1993): (a) as-processed and (b) after creep deformation at 250°C and 75 MPa. Note the interactions between dislocations and precipitates (courtesy of P. Krajewski).

experiments is shown in an inset.

The physical explanation for the threshold stress in discontinuously reinforced composites can be attributed to a variety of reasons (Dunand and Derby, 1993; Pandey et al., 1992): (1) Orowan bowing between particles, (2) back-stress associated with dislocation climb, and (3) attractive force between dislocations and particles, resulting from relaxation of the strain field of dislocations at the particle/matrix interface (Arzt and Wilkinson, 1986). Due to the higher work hardening rate of the matrix, i.e., the addition of particle decreases the volume of matrix material, increasing the word hardening rate relatively to the unreinforced alloy, the enhancement of dislocation/dislocation interactions can contribute to σ_R, although this mechanism is more plausible at ambient temperature.

A threshold stress approach cannot always be used to explain the high stress exponents observed in MMCs. Load transfer to the reinforcement, despite the lower aspect ratios of particles and whiskers, is significant. With increasing load transfer to the reinforcement, the resolved shear stress on dislocations in the matrix may be lowered significantly below that required for Orowan bowing. Dragone and Nix (1992) studied the creep behavior of Al_2O_3 short fiber reinforced Al-5% Mg alloy between 200-400°C. They also observed anomalously high values of stress exponent ($n \sim 12$-15) in the composites, while the unreinforced alloy exhibited much lower, typical values ($n \sim 3$), Fig. 9.14. The measured activation energy (225 kJ/mol) for the composites was also anomalously high. A threshold stress analysis showed that the contribution from Orowan bowing was very small. Using a model consisting of randomly oriented short fibers in the Al alloy matrix, and considering the progressive damage to the fibers during creep, they were able to predict the experimentally-observed high values of stress exponent and activation energy. Dragone and Nix (1990) also noted that the arrangement of fibers had a significant effect on the degree of matrix constraint. A decrease in effective stress (increase in matrix constraint) was observed with increasing volume fraction, fiber aspect ratio, and degree of overlap between fibers. Figure 9.15 shows a decrease in the von Mises stress in the matrix with increasing volume fraction and aspect ratio of the short fibers. The stress and strain distributions in fiber and matrix with increasing time are shown in Fig. 9.16. The stress in the fiber increases steadily with creep, indicating load transfer from the matrix to the fiber. Localization of plastic stain begins at the sharp corner of the fiber and progresses at the fiber/matrix interface normal to the loading axis. The normal and shear stresses at the fiber /matrix interface are also quite large, indicating that void growth or debonding may take place during the creep process.

Threshold Stress Analysis in Creep

The threshold stress analysis can be illustrated as follows. The figure below in part (a) (after Li and Langdon, 1998a), below, shows the experimental creep data for an Al 7005/Al_2O_3/20_p composite, in terms of shear strain rate, $\dot{\gamma}$, versus shear stress, τ, between 573-773 K. As described above, the composite exhibits an increasing stress exponent with decreasing applied stress.

The next step is to find the "true" stress exponent. This is obtained by plotting the data in terms of $\dot{\gamma}^{1/n}$ for several values of n. The plot with the best linear fit is usually a good indication of the true stress exponent. In the current case, a stress exponent of ~ 4 was obtained, part (b) (after Li and Langdon, 1998a). The exponent calculated from linear regression should be similar to that of the unreinforced alloy, where pure metallic behavior applies (unless the matrix itself has some oxide dispersions, and behaves as a dispersion strengthened material). Linear extrapolation of the linear fits to the x-axis yields the threshold stress of the material at a given temperature, τ_o.

In order to complete the analysis, the normalized creep rate is plotted versus the effective stress, part (c) (after Li and Langdon, 1998a). The normalized creep rate, from the Mukherjee-Bird-Dorn equation, is given by:

$$\frac{\dot{\gamma}kT}{D_c Gb}$$

The effective stress is the applied stress minus the threshold stress, normalized by the temperature-dependence of the shear modulus:

$$\frac{(\tau - \tau_o)}{G}$$

If the threshold stress values are correct, the above plot should "collapse" the data for all temperatures onto a single line with a slope equal to the true stress exponent.

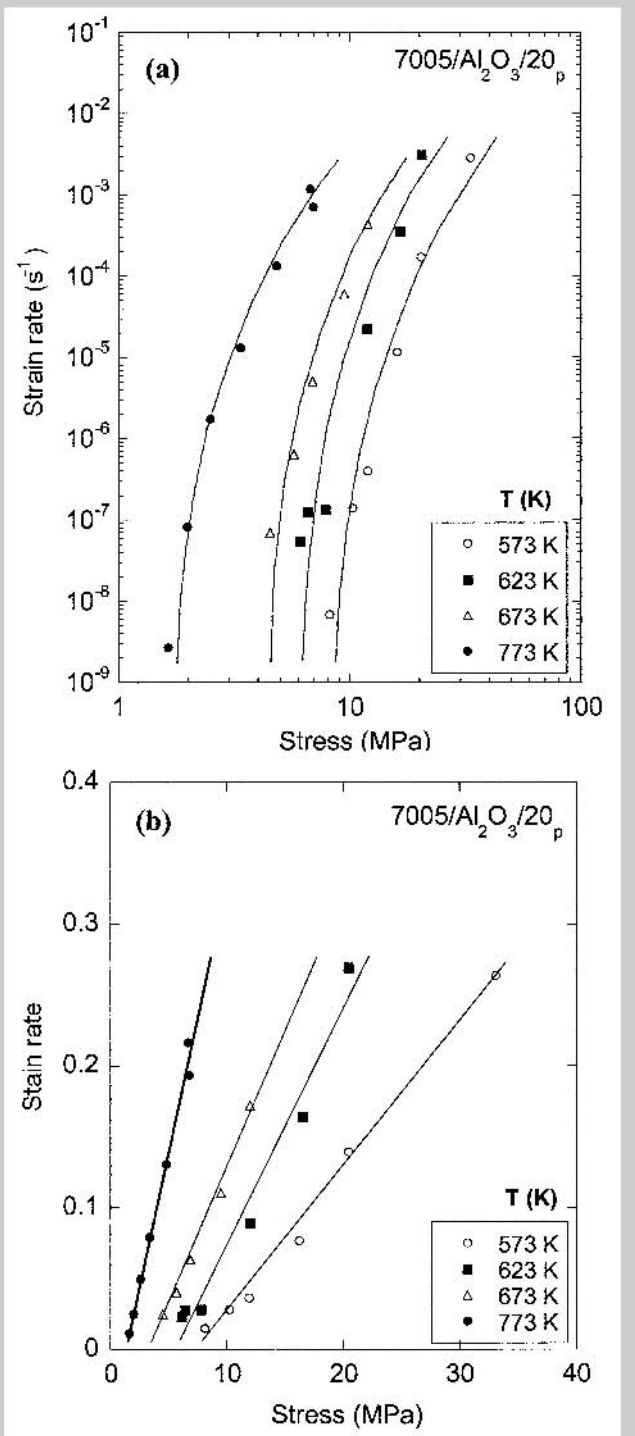
(a)
7005/Al2O3/20p
Strain rate (s-1)
Stress (MPa)
T (K)
573 K
623 K
673 K
773 K
(b)
7005/Al2O3/20p
Stain rate
Stress (MPa)
T (K)
573 K
623 K
673 K
773 K

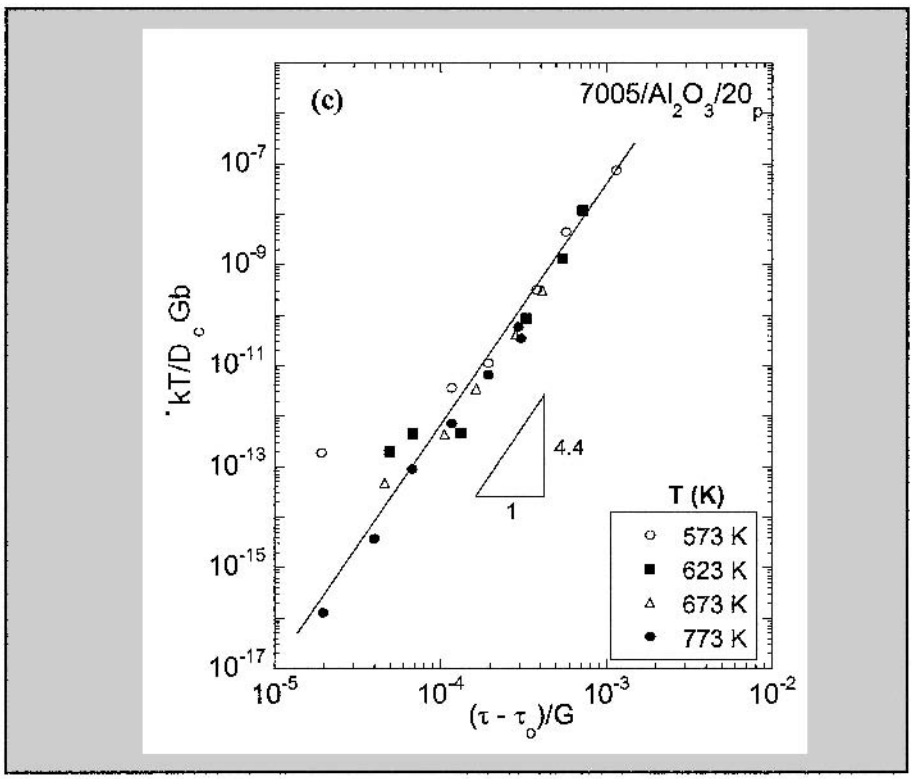

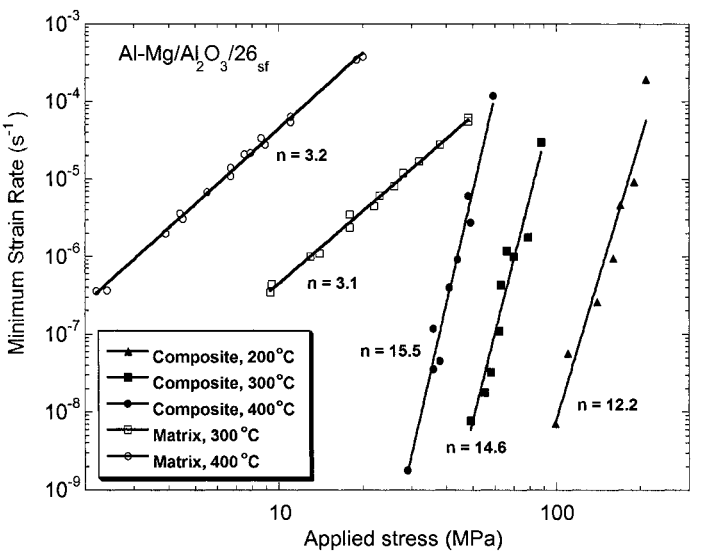

Fig. 9.14 Comparison of creep behavior of Al-5Mg/Al_2O_3/26_{sf} versus the unreinforced alloy (after Dragone and Nix, 1992). Anomalously high values of the stress exponent, n, were observed in the composite.

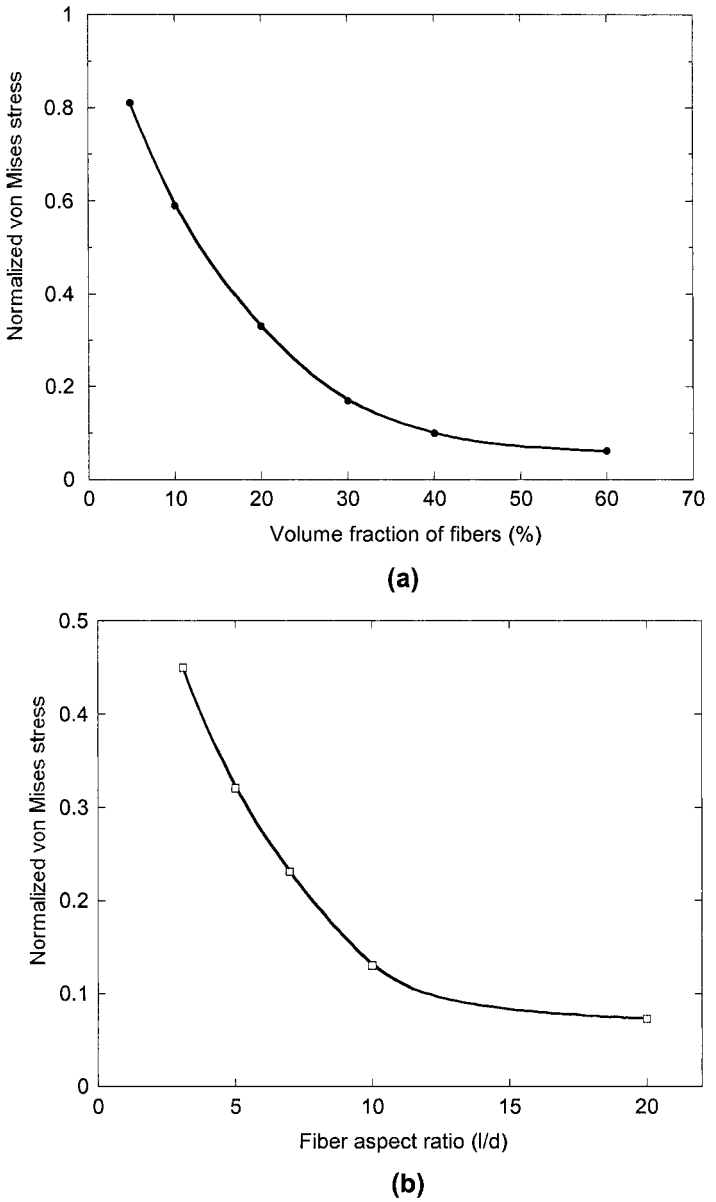

Fig. 9.15 Finite element model of creep in an Al_2O_3 short fiber reinforced Al alloy matrix composite (after Dragone and Nix, 1990). The von Mises stress in the matrix decreases with: (a) increasing volume fraction and (b) aspect ratio of the short fibers.

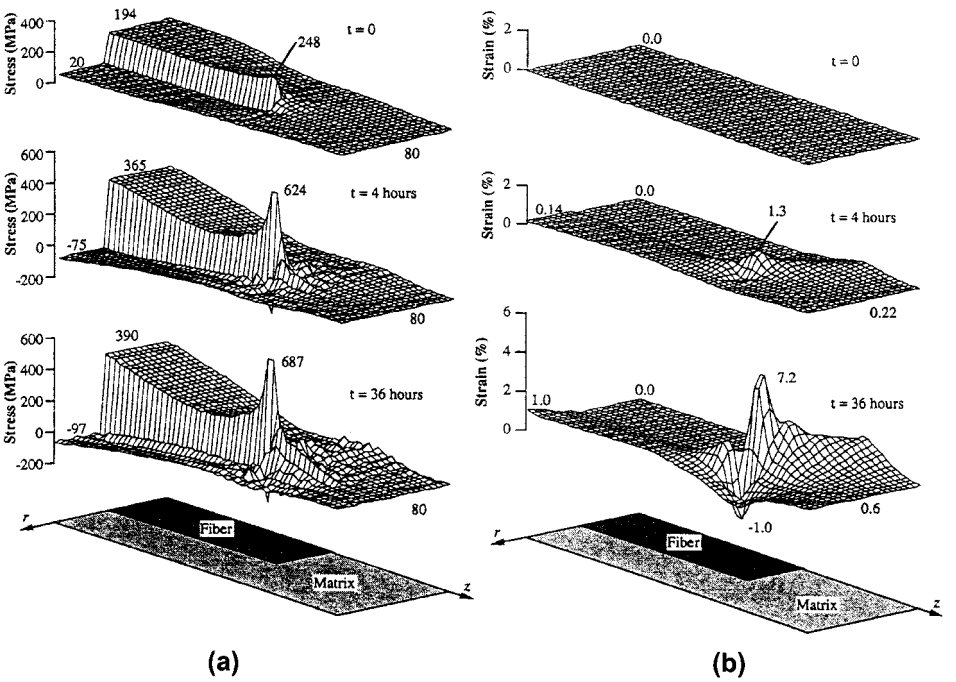

Fig. 9.16 Finite element model of creep in an Al_2O_3 short fiber reinforced Al alloy matrix composite: (a) stress distribution and (b) strain distribution during, with increasing time (after Dragone and Nix, 1990; courtesy of W.D. Nix). The stress in the fiber increases steadily with creep, indicating load transfer from the matrix to the fiber. Localization of plastic stain begins at the sharp corner of the fiber and progresses at the fiber/matrix interface normal to the loading axis.

Other continuum-based unit-cell approaches have also been used to model creep of discontinuously reinforced metal matrix composites (Bao et al., 1991; Davis and Allison, 1995; Atkins and Gibeling, 1995; Biner, 1996). Assuming a spherical particle and the power-law creep formulation for the metal matrix, Davis and Allison (1995) showed that the ratio of composite to matrix steady-state creep rates depends primarily on the volume fraction and geometry of the reinforcing phase, with the stress exponent of the composite and that of the matrix remaining relatively constant. The higher resistance to creep in the composite is largely attributed to the constrained matrix flow, leading to a reduced creep rate in the composite. Changes in modulus ratio of reinforcement to matrix affected the initial stress distribution and creep rates, but did not really affect the final creep rates. Higher modulus mismatch between reinforcement and matrix resulted in higher initial creep rates. Residual stresses due to thermal expansion mismatch also resulted in higher initial creep rates in the composite.

Other aspects of creep deformation, such as grain boundary sliding have also been included (Biner, 1996). It was shown that when the grains in the matrix were allowed to slide, that incorporation of the reinforcement resulted in an enhancement in stress in the matrix (described above) which can result in inhomogeneous grain boundary sliding. Figure 9.17(a) shows the evolution of grain boundary cavitation and sliding in a short fiber reinforced metal matrix composite. As described above, the strain concentration takes place at the pole of the reinforcement, which coincides with the onset of matrix grain cavitation. With increasing time, grain boundary sliding takes place at the cavities or facet cracks. This effect is accentuated with an increase in reinforcement aspect ratio, Fig. 9.17(b), as the local strain concentration in the matrix, immediately above the reinforcement, increases. Figure 9.18 shows a comparison of predicted creep rates for (i) matrix exhibiting cavitation and sliding, (ii) composite exhibiting matrix cavitation and sliding, and (iii) composite exhibiting matrix cavitation without sliding. The unreinforced alloy has a higher creep rate than the composite. The composite with matrix sliding but no cavitation exhibits slower creep rates at lower stress, but the creep rates approach that of the matrix at relatively large stress.

It has also been observed that below a critical strain rate diffusional relaxation around the SiC particles is the rate-controlling mechanism, while above this point, a greater degree of load is carried by the high stiffness particles (Zong and Derby, 1997). In addition to the threshold stress, additional proposed mechanisms for the anomalously high values of Q and n include power law break-down of the matrix (Zong and Derby, 1997; Lilholt, 1985) and interfacial decohesion at the particle/matrix interface (Taya and Lilholt, 1986). The reinforcement may contribute to changes in the matrix during creep by localized recrystallization at corners or interfaces and precipitate coarsening at the particle/matrix interface, where the density of precipitates is the highest (because of the greatest thermal mismatch stress upon cooling being at the interface).

It is interesting to note that in powder processed composite materials, oxide dispersions (not present in the unreinforced alloy) may also contribute to extremely high "anomalous" values of n and Q (Park et al., 1990; Li and Langdon, 1998b). Park et al. (1990) suggested that the presence of fine oxide particles, incoherent with the matrix, arising from the powder metallurgy process used to fabricate the composite, served as effective barriers for dislocation motion and gave rise to a threshold creep stress. The high creep stress exponent and increase in exponent with decreasing applied stress were attributed to the oxide particles in the matrix. The work of Li and Langdon

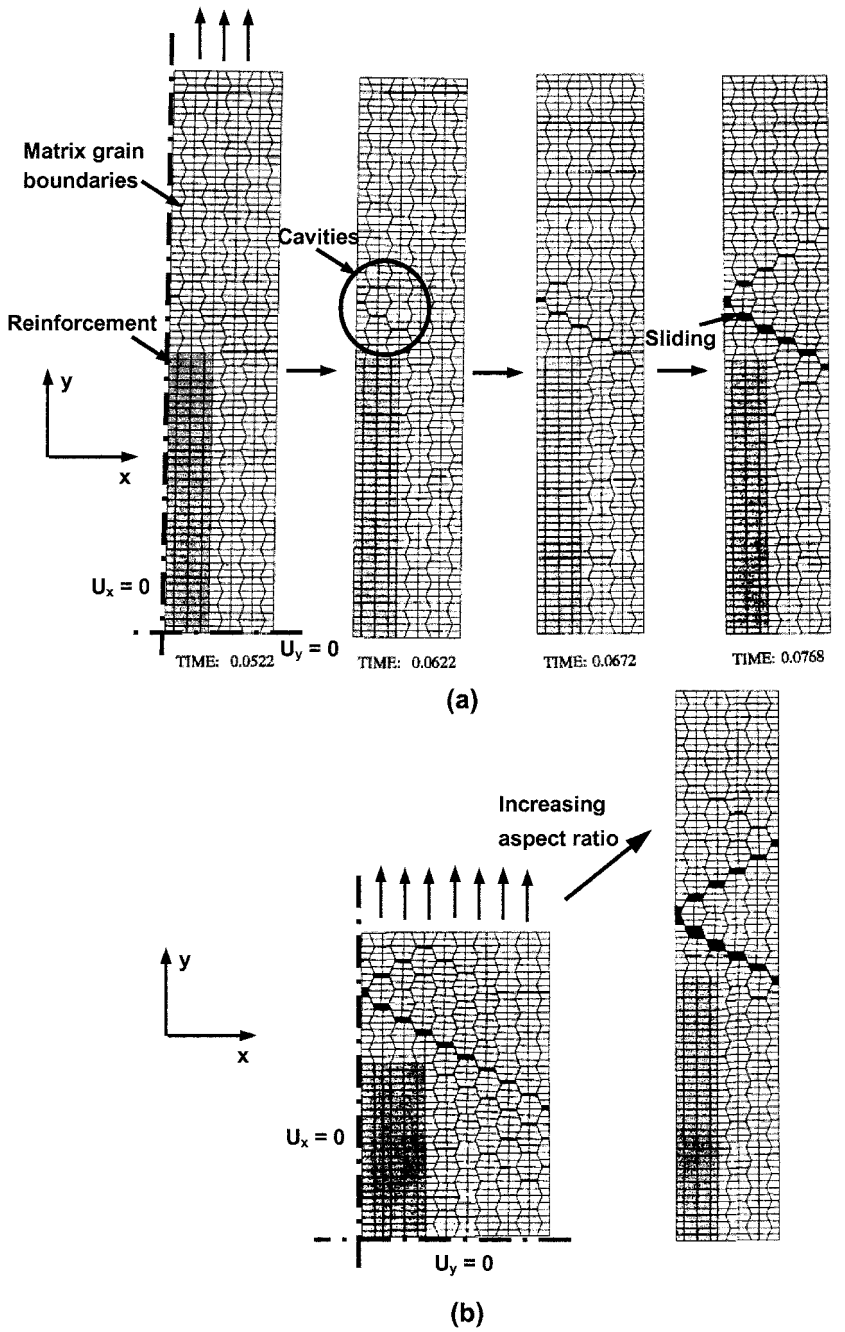

Fig. 9.17 (a) Finite element modeling of grain boundary cavitation and sliding in a short fiber reinforced metal matrix composite (after Biner, 1996; courtesy of S. Biner). Strain concentration takes place at the pole of the reinforcement, which coincides with the onset of matrix grain cavitation. With increasing time, sliding takes place at the cavities or facet cracks. (b) Increase in reinforcement aspect ratio accentuates local strain concentration in the matrix.

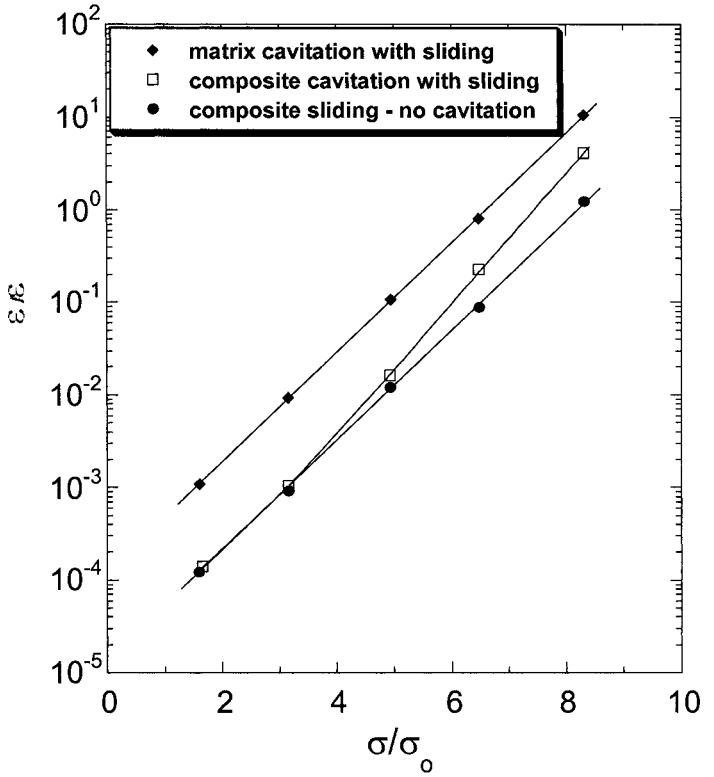

Fig. 9.18 Finite element model comparison of predicted creep rates for (i) matrix exhibiting cavitation and sliding, (ii) composite exhibiting matrix cavitation and sliding, and (iii) composite exhibiting matrix cavitation without sliding (after Biner, 1996). The unreinforced alloy has a higher creep rate than the composite. The composite with matrix sliding but no cavitation exhibits slower creep rates at lower stress, but the creep rates approach that of the matrix at relatively large stress.

(1998a) supports this conclusion. They add that in composites processed via ingot metallurgy, compared to powder metallurgy-processed composites of the same composition, viscous glide is the rate-controlling mechanism because of the absence of oxide particles.

Li and Langdon (1998a) also proposed two separate classes of creep behavior in metal matrix composites. In class M (pure metal type) materials dislocation climb is the rate-controlling mechanism, with a stress exponent of around 5 and activation energy similar to the value for self-diffusion in the matrix. In class A (alloy type) metals, viscous dislocation glide is the rate-controlling mechanism, with a stress exponent of around 3 and an activation energy associated with the viscous drag of the solute atmospheres.

Exceptionally high creep rates were observed at the highest stress levels, perhaps due to dislocations breaking away from solute atom atmospheres (Li and Langdon, 1998b). It should be noted that in unreinforced solid solution alloys a transition occurs between class M behavior at low stresses to class A behavior at higher stresses (Yavari et al., 1981).

Li and Langdon (1998a) derived an expression which can be used to determine the transition in material behavior from class M to class A:

$$\alpha\left(\frac{kT}{ec^{1/2}Gb^3}\right)^2 = B\left(\frac{\Gamma}{Gb}\right)^3\left(\frac{D_c}{D_g}\right)\left(\frac{\sigma_e}{G}\right)^2$$

where σ_e is the effective stress, β is a constant associated with the relative contributions from various viscous glide processes, e is the solute-solvent size mismatch, Γ, is the stacking fault energy of the matrix, B is a constant, and D_c and D_g, are the diffusion coefficients for dislocation climb and glide, respectively. A graphical representation of this equation, for several material systems, is shown in Fig. 9.19.

9.3 SUPERPLASTICITY

Superplasticity can be defined as the ability of a material to undergo uniform very large plastic strains (> 100% strain) (Meyers and Chawla, 1999). The

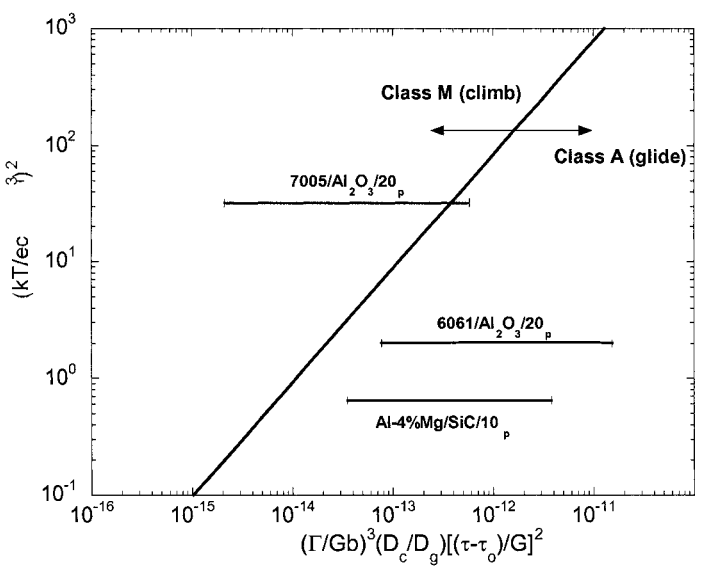

Fig. 9.19 Graphical representation of the trasition from class M (pure metal type) behavior class A (alloy type) behavior (after Li and Langdon, 1998a).

stress (σ)-strain rate ($\dot{\varepsilon}$) behavior of most materials can be described by the following equation:

$$\sigma = K\dot{\varepsilon}^m$$

where K and m are constants, and m is termed the strain-rate sensitivity. For a newtonian viscous solid, m = 1. Thus, any enhancement in m will contribute to an enhancement in superplasticity. In most alloys, the microstructural requirement for a high value of m is a very fine grain size. This is because the large plastic strains attained in superplasticity are accommodated by grain boundary sliding (Ahmed and Langdon, 1977; Mohamed et al., 1977).

Superplasticity has been demonstrated in particle reinforced metal matrix composites, such as SiC particle or whisker reinforced Al. Because of the lower ductility and higher strain hardening rates in these materials, conventional superplasticity by reduction in grain size is not feasible. Wu and Sherby (1984) used thermal cycling to generate internal stresses in the composite, due to thermal expansion mismatch between reinforcement and matrix. The internal stresses assisted plastic flow and increased the m exponent. Nieh et al. (1984) conducted isothermal forming in the solid-liquid region of the material, and were able to obtain 300% strain at relatively high strain rates (~ $3x10^{-1}$/s). Mahoney and Ghosh (1987) studied the superplastic behavior of an Al-Zn-Mg-Cu matrix composite with SiC particles (about 5 μm in diameter). They were able to achieve superplastic strains of 500% in the composite, compared to 800 % in the unreinforced alloy. Fig. 9.20 shows a plot of flow stress versus strain rate during superplasticity at 516°C. An increase in SiC volume fraction resulted in an increase in the flow stress necessary for superplasticity. The flow stress versus strain rate behavior was divided into three regions, Fig. 9.21. The expected behavior of the composite is given by the dashed line. The measured flow stress, however, particularly in Region I, is much higher than the expected behavior. This was attributed to a threshold stress due to pinning of grain boundaries by the SiC particles. In Region II, the strain rate sensitivity is the highest (highest value of m), while in Region III, superplasticity is controlled by dislocation creep in the matrix.

The measured activation energies during superplasticity are often higher than for lattice diffusion or grain boundary diffusion. Li and Langdon (1998c) showed that by incorporating the contribution of load transfer to the particles (through a threshold stress approach), the true activation energy was similar to that for grain boundary diffusion. Mishra et al. (1997) studied the

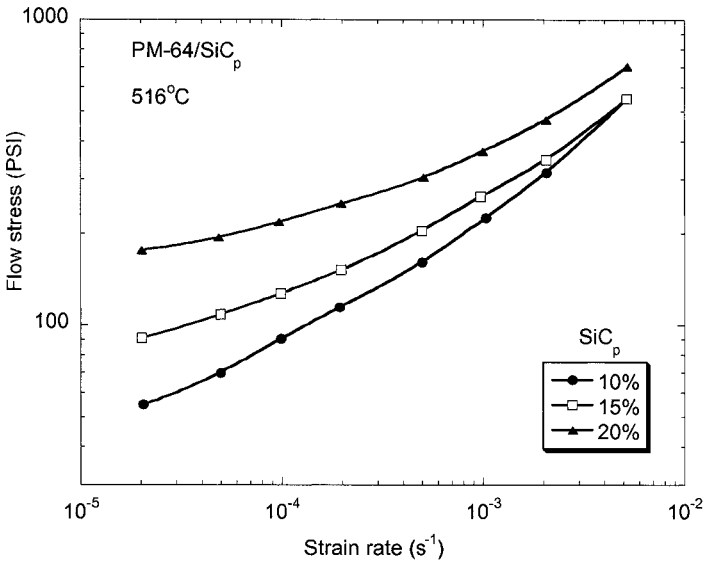

Fig. 9.20 Slow stress versus strain rate during superplasticity at 516°C of an Al alloy matrix composites reinforced with SiC particles (after Mahoney and Ghosh, 1987). An increase in SiC volume fraction resulted in an increase in the flow stress necessary for superplasticity.

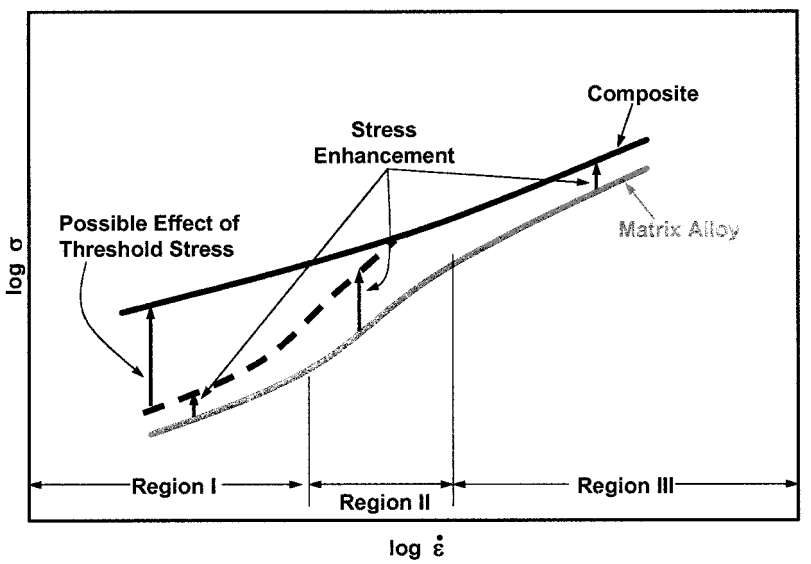

Fig. 9.21 Schematic of flow stress versus strain rate behavior for MMCs and unreinforced alloy (after Mahoney and Ghosh, 1987). The expected behavior of the composite is given by the dashed line. The measured flow stress, particularly in Region I, is much higher than the expected behavior. In Region II, the strain rate sensitivity is the highest (highest value of m), while in Region III, superplasticity is controlled by dislocation creep in the matrix.

mechanisms for superplasticity in Si_3N_4 particle reinforced 2124 Al matrix composites. In single phase materials, slip accommodation is provided by grin boundary sliding. In dispersion strengthened systems, where fine second phase particles are introduced, they pin the grain boundaries, so local diffusional relaxation around the particles must take place. In particle reinforced MMCs, however, the particles are larger than that in dispersion strengthened systems, so sliding is controlled by diffusional accommodation at the particle/matrix interface. If strain accommodation does not take place, then cavitation will occur. Mahoney and Ghosh (1987) showed that for an increase in reinforcement fraction, the fraction of voids increases, for a given applied strain, Fig. 9.22(a). This can be explained by the increase in triaxiality of stress in the matrix due to the presence of rigid, non-deforming particles (see chapter 7).

The onset of cavitation can be delayed by the superposition of a compressive hydrostatic pressure, which counteracts the triaxial tensile stress (Vasudevan et al., 1989; Lewandowski and Lowhaphandu, 1998). Figure 9.22(b) shows the delay in the onset of void growth, during superplasticity, by the superposition of a hydrostatic pressure. Mabuchi and Higashi (1999) suggested that a liquid phase during superplasticity my also decrease local stress concentrations and delay the onset of superplasticity. A large fraction of liquid phase is not desirable, however, since it will form a brittle intermetallic between the particle and matrix (see chapter 5), and cavitation will take place (Mishra et al., 1997).

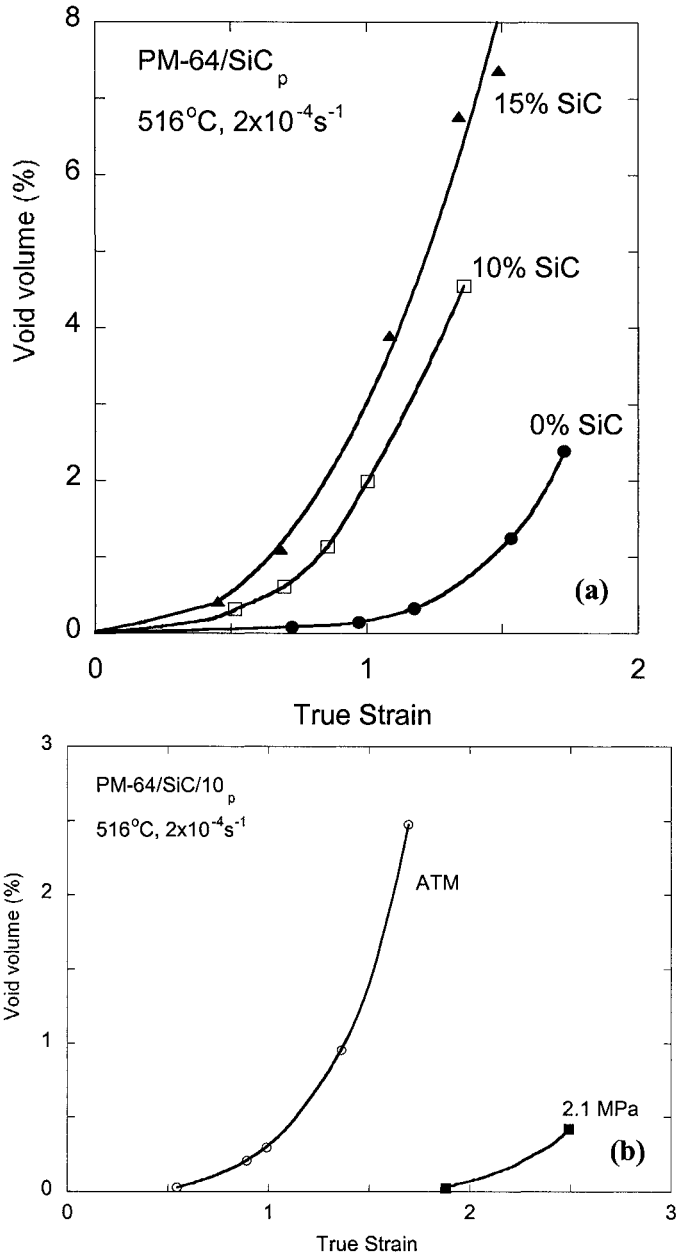

Fig. 9.22 (a) Increase in degree of cavitaiton (void volume) with increase in SiC particles in an Al alloy matrix composite (after Mahoney and Ghosh, 1987). If strain accommodation does not take place, then cavitation will occur. The increase in traixiality of stress in the matrix due to the presence of rigid, non-deforming particles results in cavitation. (b) Delay in the onset of cavitation results when a compressive hydrostatic pressure is superimposed, which counteracts the triaxial tensile stress.

References

Ahmed, M.M.I., and T.G. Langdon, (1977) *Metall. Trans.*, **8**, 1832.
Arzt, E., and D.S. Wilkinson, (1986) *Acta Metall Mater.*., **34**, 1893-1898.
Atkins, S.L., and J.C. Gibeling, (1995) *Metall. Mater. Trans.*, **26A**, 3067-3079.
Bao, G., J.W. Hutchinson, and R.M. McMeeking, (1991) *Acta Metall. Mater.*, **39**, 1871-1882.
Biner, S.B., (1996) *Acta Mater.*, **44**, 1813-1829.
Bullock, E., M. McLean, and D.E. Miles, (1977) *Acta Metall.*, **25**, 333-344.
Davies, P.W., G. Nelmes, K.R. Williams, and B. Wilshire, (1973) *Metal Sci. J.*, **7**, 87-92.
Davis, L.C., and J.E. Allison, (1995) *Metall. Mater. Trans.*, **26A**, 3081-3089.
Dlouhy, A., N. Merk, and G. Eggeler, (1993) *Acta Metall. Mater.*, **41**, 3245-3256.
Dlouhy, A., G. Eggeler, and N. Merk, (1995) *Acta Metall. Mater.*, **43**, 535-550.
Dragone, T.L., and W. D. Nix, (1990) *Acta Metall. Mater.*, **38**, 1941.
Dragone, T.L., and W. D. Nix, (1992) *Acta Metall. Mater.*, **40**, 2781.
Dunand, D.C., and B. Derby, (1993) in *Fundamentals of Metal Matrix Composites*, (S. Suresh, A. Mortensen, and A. Needleman, eds.), Butterworth-Heinneman, Boston, pp. 191-214.
Evans, R.W., and B. Wilshire, (1993) *Introduction to Creep*, The Institute of Materials, London.
Goto, S., and M. McLean, (1989) *Scripta Mater.*, **23**, 2073-2078.
Goto, S., and M. McLean, (1991) *Acta Metall. Mater.*, **39**, 153-164.
Kerr, M., and N. Chawla, (2004) *Acta Mater.*, **52** 4527-4535.
Krajewski, P.E., J.E. Allison, and J.W. Jones, (1993) *Metall. Trans.*, **24A**, 2731-2741.
Krajewski, P.E., J.E. Allison, and J.W. Jones, (1995) *Metall. Mater. Trans.*, **26A**, 3107-3118.
Lee, S., S.M. Jeng, and J.-M. Yang, (1995) *Mech. Mater.*, **21**, 303-312.
Lewandowski, J.J, and P. Lowhaphandu, (1998) *Int. Mater. Rev.*, **43**, 145-187.
Leyens, C., J. Hausmann, and J. Kumpfert, (2003) *Adv. Eng. Mater.*, **5**, 399-410.
Li, Y., and T.G. Langdon, (1998a) *Acta Mater.*, **46**, 1143-1155.
Li, Y., and T.G. Langdon, (1998b) *Mater. Sci. Eng.*, **A245**, 1-9.
Li, Y., and T.G. Langdon, (1998c) *Acta Mater.*, **46**, 3937-3948.
Lilholt, H., (1985) *Comp. Sci. Tech.*, **22**, 277-294.
Lilholt, H., (1991) *Mater. Sci. Eng.*, **A135**, 161-171.
Mabuchi, M., and K. Higashi, (1999) *Acta Mater.*, **47**, 1915-1922.

Mahoney, M., and A.K. Ghosh, (1987) *Metall. Trans.*, **18A**, 653-661.
Meyers, M.A., and K.K. Chawla, (1999) *Mechanical Behavior of Materials*, Prentice Hall, Upper Saddle River, NJ, pp. 540-591.
Mishra, R.S., T.R. Bieler, and A.K. Mukherjee, (1997) *Acta Mater.*, **45**, 561-568.
Mohamed, F.A., M.M.I. Ahmed, and T.G. Langdon, (1977) *Metall. Trans.*, **8**, 933.
Mukherjee, A.K., J.E. Bird, and J.E. Dorn, (1964) *Trans. ASM*, **62**, 155.
Nardone, V.C., and J.R. Strife, (1987) *Metall. Trans.*, **18A**, 109-114.
Nardone, V.C., and J.K. Tien, (1986) *Scripta Mater.*, **20**, 797-802.
Nieh, T.G., (1984) *Metall. Trans.*, **15A**, 139-146.
Nieh, T.G., C.A. Henshall, and J. Wadsworth, (1984) *Scripta Metall.*, **18**, 1405-1408.
Ohno, N., K. Toyoda, N. Okamoto, T. Miyake, and S. Nishide, (1994) *Trans. ASME*, **116**, 208-214.
Pandey, A.B., R.S. Mishra, and Y.R. Mahajan, (1992) *Acta Metall. Mater.*, **40**, 2045-2052.
Park, K.-T., E.J. Lavernia, and F.A. Mohamed, (1990) *Acta Metall. Mater.*, **38**, 2149-2159.
Parker, J.D., and B. Wilshire, (1975) *Metal Sci. J.*, **9**, 248-252.
Sherby, O.D., R.H. Klundt, and A.K. Miller, (1977) *Metall. Trans.*, **8A**, 843-850.
Sørensen, N, A. Needleman, and V. Tvergaard, (1992) *Mater. Sci. Eng.*, **A158**, 129-137.
Taya, M., and H. Lilholt, (1986) in *Advances in Composite Materials and Structures* (S.S. Wang and Y.D.S. Rajapakse, eds.), ASME, New York, 21-27.
Vasudevan, A.K., O Richmond, F. Zok, and J.D. Embury, (1989) *Mater. Sci. Eng.*, **A107**, 63-69.
Webster, D., (1982) *Metall. Mater. Trans.*, **13A**, 1511-1519.
Whitehouse, A.F., H.M.A. Winand, and T.W. Clyne, (1998) *Mater. Sci. Eng.*, **A242**, 57-69.
Wu, M.Y., and O.D. Sherby, (1984) *Scripta Metall.*, **18**, 773-776.
Yavari, P., F.A. Mohamed, and T.G. Langdon, (1981) *Acta Metall.*, **29**, 1495.
Zong, B.Y., and B. Derby, (1997) *Acta Mater.*, **45**, 41-49.